Invited Paper

Fast and Robust Deconvolution-Based Image Reconstruction for Photoacoustic Tomography in Circular Geometry: Experimental Validation

C. Zhang
C. Li
L. V. Wang, Fellow, IEEE
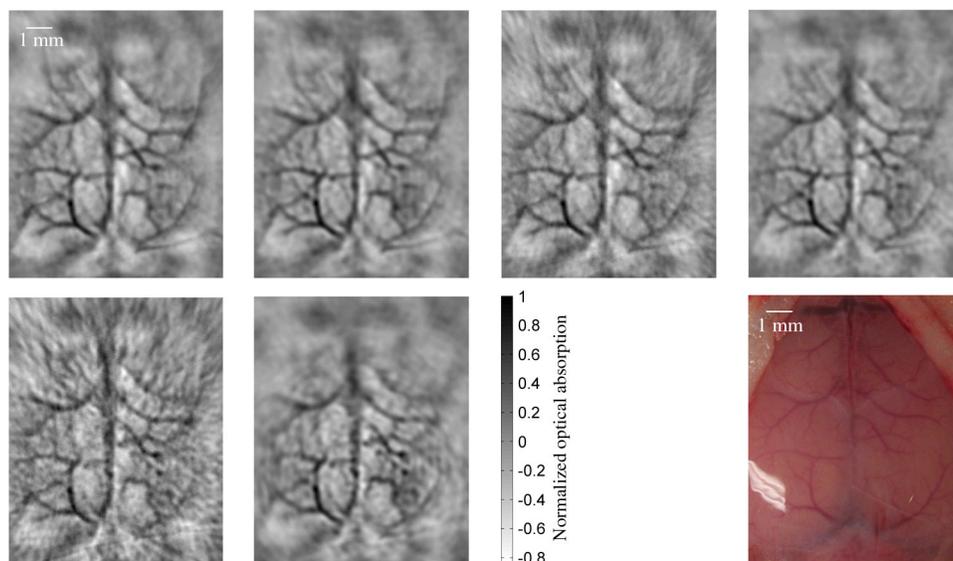
Fast and Robust Deconvolution-Based Image Reconstruction for Photoacoustic Tomography in Circular Geometry: Experimental Validation

Chi Zhang, Changhui Li, and Lihong V. Wang, *Fellow, IEEE*

(Invited Paper)

Optical Imaging Laboratory, Department of Biomedical Engineering,
Washington University in St. Louis, St. Louis, MO 63130-4899 USA

Abstract: Photoacoustic tomography (PAT) is a fast-developing biomedical imaging technology suitable for *in vivo* imaging. PAT in spherical or circular geometry gives good image resolution yet is slow or expensive in signal acquisition and image formation. Reducing the number of detection angles can ameliorate such issues, usually at the expense of image quality. This paper introduces a deconvolution-based algorithm that models the imaging process as a linear and shift-invariant system. As demonstrated by the *in vivo* experiment, this algorithm not only runs much faster than the back-projection algorithm but also shows stronger robustness in that it provides better image quality when detection angles are sparse. Therefore, this algorithm promises to enable real-time PAT in circular geometry.

Index Terms: Photoacoustic tomography, deconvolution reconstruction, sparse detection angles, real-time imaging, circular geometry.

1. Introduction

In the past decade, photoacoustic tomography (PAT) has emerged as a fast-developing biomedical imaging technology [1], [2]. Based on the photoacoustic (PA) effect [3], PAT utilizes a laser source to illuminate tissue and then detects the generated acoustic signals for imaging. PAT offers advantages in many aspects. First, PAT uses nonionizing illumination that poses no health hazard and is noninvasive. Second, as a hybrid of optical and ultrasound imaging techniques, PAT combines the merits of both. It provides high optical contrast and good ultrasonic resolution, breaks through the depth limit at the optical transport mean free path ($\sim$1 mm), and does not suffer from ultrasound speckles. Third, since optical absorption is strongly related to physiological status, such as oxygen saturation and concentration of hemoglobin, PA signals contain functional information. Accordingly, in recent years PAT has been successfully applied to *in vivo* blood vessel imaging [4], [5] and brain structural and functional imaging [6]–[8] of small animals. Thermoacoustic tomography (TAT) is another important PA-based imaging technology. Utilizing a microwave illumination source, TAT can image deeper than PAT and is especially suitable for breast tumor imaging [9]–[11].

To enable the reconstruction of 3-D tissue structures in PAT, spherical, planar, and cylindrical geometries are normally used in PA signal acquisition. In most applications, they are reduced to circular and linear geometries to image a 2-D tissue cross section. Linear detection geometry normally provides poorer image quality than circular geometry, because of its limited view of detection. Yet, linear geometry is widely used because it is easily applicable to various tissue shapes and can lead to fast, or even real-time, imaging [4], [12] by using a linear transducer array and corresponding fast algorithms [13], [14]. Circular geometry offers full-view detection and hence good image resolution. However, imaging in such geometry is usually very slow for two reasons: the long signal acquisition time (introduced by rotating a single-element transducer around the tissue) and the large time cost of the reconstruction algorithms (either the commonly used exact back-projection algorithm [15] or the simple delay-and-sum algorithm [16]). The former can be overcome by using a ring-shaped transducer array [17], but the latter, to the best of our knowledge, still remains a problem. For example, the 512-element-array-based PAT system reported in [17] can achieve real-time signal acquisition but not real-time image formation.

A possible solution is to reduce the number of detection angles in circular geometry, which will decrease not only image reconstruction time but will also signal acquisition time or equipment cost. Nevertheless, for most algorithms the quality of the reconstructed image is strongly related to the number of detection angles. In many cases, 128 angles or fewer may result in strong artifacts in the reconstructed image. The compressed sensing algorithm can be utilized to improve image quality [18], but this algorithm is in essence an optimization approach that requires iterative calculation and, therefore, is not suitable for fast or real-time imaging.

In this paper, we introduce the deconvolution reconstruction (DR) algorithm for PAT in 3-D spherical geometry and 2-D circular geometry. The DR algorithm is very fast since its key step is the Fourier-based deconvolution. Moreover, the DR algorithm renders better image quality than other popular algorithms when using a small number of detection angles. Therefore, the DR algorithm promises to enable real-time imaging in circular geometry. We have previously published basic formulas and simulation results of the DR algorithm to show that it has good precision and is insensitive to data noise [19]. Here, the DR algorithm is systematically described and then verified by experimental data with an emphasis on the case of sparse detection angles.

The paper is organized as follows. First, a brief description of the PA forward problem and solution is provided. Then, the DR algorithm is derived mathematically and explained physically. *In vivo* experimental results on the mouse cerebral cortex are then presented to validate this algorithm.

2. Forward Solution

The PA theory, as summarized in [20], is briefly described here. The relation between the illuminating light and the excited acoustic wave in an inviscid medium obeys the following wave equation:

$$\nabla^2 p(\mathbf{r}, t) - \frac{1}{c^2} \frac{\partial^2}{\partial t^2} p(\mathbf{r}, t) = -\frac{\beta}{C_p} A(\mathbf{r}) \frac{\partial I(t)}{\partial t} \tag{1}$$

where $A(\mathbf{r})$ is the absorbed energy density, $p(\mathbf{r}, t)$ is the excited acoustic pressure, $\mathbf{r}$ is the 3-D position vector, t is the time, $I(t)$ is the illumination pulse function, c is the sound speed, β is the coefficient of volumetric thermal expansion, and C_p is the specific heat.

$I(t)$ is usually assumed to be a delta function, and c is assumed to be constant. PA signals are detected along a sphere, which is defined by $\mathbf{r}_d$, whose radius is r_d and whose center is the origin. Then, by using Green's functions, the detected PA signal $p(\mathbf{r}_d, t)$ can be expressed as

$$p(\mathbf{r}_d, t) = \frac{\beta}{4\pi C_p} \frac{\partial}{\partial t} \oiint_{|\mathbf{r}' - \mathbf{r}_d| = ct} \frac{A(\mathbf{r}')}{t} d^2\mathbf{r}'. \tag{2}$$

In practical experiments, each detected signal is convolved by both the illumination pulse and the transducer impulse response. We can get a better estimation of $p(\mathbf{r}_d, t)$ by deconvolving the signal if the impulse response is known and the signal-to-noise ratio is sufficiently high. Then, image reconstruction is an inverse problem of calculating $A(\mathbf{r})$ from $p(\mathbf{r}_d, t)$, which is solved algorithmically.

3. DR Algorithm

The basic idea of the DR algorithm is to construct a 3-D system. When the system input is $A(\mathbf{r})$, the output will be a 3-D space function that is related to $p(\mathbf{r}_d, t)$. By reasonable design, this system can be constructed to be linear and shift invariant. Then, $A(\mathbf{r})$ can be calculated by deconvolution. In this section, we will give the 3-D formulation, physical meaning, and 2-D discrete implementation (with time complexity analysis) of the DR algorithm.

3.1. Formulation

Fundamental formulas of the DR algorithm are presented here. See [19] for more details.
Let us define

$$S(\mathbf{r}_d, t) = \left[\int_0^t p(\mathbf{r}_d, t) \, dt \right] \cdot t. \tag{3}$$

Substituting (2) into (3) leads to

$$S(\mathbf{r}_d, t) = \eta \oiint_{|\mathbf{r}' - \mathbf{r}_d| = ct} A(\mathbf{r}') \, d^2\mathbf{r}' \tag{4}$$

where $\eta = \beta/(4\pi C_p)$.

In order to construct the linear and shift-invariant system, we start by constructing the system output from $p(\mathbf{r}_d, t)$ when the input is $A(\mathbf{r})$. The output function $C(\mathbf{r})$ is constructed as

$$C(\mathbf{r}) = S\left(\frac{\mathbf{r}}{|\mathbf{r}|} \cdot r_d, \, t_{max} - \frac{|\mathbf{r}|}{c} \right) \tag{5}$$

where t_{max} is an adjustable parameter. PA signals during time 0–t_{max} are used to construct $C(\mathbf{r})$. In order to cover the major information in PA signals, normally, it should be satisfied that $ct_{max} \geq 2r_d$. $C(\mathbf{r})$ is zero when $|\mathbf{r}| > ct_{max}$.

Substituting (4) into (5) leads to

$$C(\mathbf{r}) = \eta \oiint_{\Omega} A(\mathbf{r}') \, d^2\mathbf{r}' \tag{6}$$

where the integral surface Ω can be expressed as

$$\left| \mathbf{r}' - \frac{\mathbf{r}}{|\mathbf{r}|} \cdot r_d \right| = ct_{max} - |\mathbf{r}|. \tag{7}$$

Considering that the detected tissue is contained by the sphere $\mathbf{r}_d$, $A(\mathbf{r}')$ has nonzero values only if $|\mathbf{r}'| < r_d$ (which means $A(\mathbf{r}')$ needs to be integrated only over Ω within this region). Further, $2|\mathbf{r}'| < ct_{max} - r_d$ if ct_{max} is greater than $3r_d$, or the tissue volume is relatively small. If each ultrasonic detector receives PA signals within a sufficiently small solid angle, (7) can be approximated to the following surface by using the Taylor series expanded to the first order [19]:

$$|\mathbf{r}' - \mathbf{r}| = ct_{max} - r_d. \tag{8}$$

The smaller the maximum of $|\mathbf{r}'|$ is, the smaller the ignored higher order Taylor polynomials. In other words, a smaller tissue volume in comparison to the detection radius results in less error. Thus, (6) can be approximated as

$$C(\mathbf{r}) = \eta \oiint\limits_{|\mathbf{r}'-\mathbf{r}|=ct_{max}-r_d} A(\mathbf{r}')d^2\mathbf{r}'. \tag{9}$$

Now, the relationship between $A(\mathbf{r})$ and $C(\mathbf{r})$ is clear. The constructed system as described by (9) can be easily shown to be linear and shift invariant. In other words, if $A(\mathbf{r}')$ is shifted spatially by $\Delta\mathbf{r}$, the response $C(\mathbf{r})$ will be shifted by the same distance in the same direction because $|\mathbf{r}' - \mathbf{r}| = ct_{max} - r_d$ must hold. Therefore, (9) can be rewritten as

$$C(\mathbf{r}) = A(\mathbf{r}) * h(\mathbf{r}) \tag{10}$$

where $h(\mathbf{r})$ is the system impulse response—the response of the constructed system to a point PA source located at the origin—and $*$ represents 3-D convolution. When the system input is the 3-D delta function, $h(\mathbf{r})$ is the system output

$$h(\mathbf{r}) = \eta \oiint\limits_{|\mathbf{r}'-\mathbf{r}|=ct_{max}-r_d} \delta^3(\mathbf{r}')d^2\mathbf{r}' \tag{11}$$

or

$$h(\mathbf{r}) = \eta\delta(|\mathbf{r}| - ct_{max} + r_d). \tag{12}$$

Based on (10), $A(\mathbf{r})$ can be calculated by a simplified Wiener deconvolution method [21]

$$\widetilde{A}(\omega) = \frac{\widetilde{C}(\omega)}{\widetilde{h}(\omega) \cdot \left(1 + \lambda/|\widetilde{h}(\omega)|^2\right)} \tag{13}$$

where $\widetilde{A}(\omega)$, $\widetilde{h}(\omega)$, and $\widetilde{C}(\omega)$ are the 3-D Fourier transforms of $A(\mathbf{r})$, $h(\mathbf{r})$, and $C(\mathbf{r})$, respectively; and λ is a constant (adjustable according to applications).

To summarize, the DR algorithm consists of two steps: First, construct $C(\mathbf{r})$ based on (3) and (5); second, calculate $A(\mathbf{r})$ by (13). It is worth noting again that DR is an approximate algorithm because (9) is approximated from (6). Smaller tissue volumes in comparison with the detection radius result in less error. It has also been shown that the optimal value of t_{max} is $2r_d/c$ (as used in the following experiments), where DR provides the fastest calculation while maintaining good image quality [19].

3.2. Physical Meaning

The physical meanings of the key formulas in this DR algorithm are explained here. The function $S(\mathbf{r}_d, t)$, as defined in (3), can be understood as the processed time-domain PA signal, which is proportional to the velocity potential multiplied by the time of arrival [20]. It is due to the integration of $A(\mathbf{r})$ over a spherical shell, as shown in (4). Then $S(\mathbf{r}_d, t)$ is transformed to $C(\mathbf{r})$ by (5). The value of $C(\mathbf{r})$ at position $\mathbf{r}$ corresponds to the signal S processed from the pressure p received by the $\mathbf{r}$-direction transducer, located at position $\mathbf{r} \cdot r_d/|\mathbf{r}|$, at time $(ct_{max} - |\mathbf{r}|)/c$. In other words, the value of $C(\mathbf{r})$ at position $\mathbf{r}$ corresponds to the tissue lying on a spherical surface whose center is $\mathbf{r} \cdot r_d/|\mathbf{r}|$ and whose radius is $ct_{max} - |\mathbf{r}|$, as shown in Fig. 1. This transformation allows us to merge two variables $(\mathbf{r}_d, t)$ into a single variable $\mathbf{r}$.

According to (10), $C(\mathbf{r})$ approximates to the convolution of $A(\mathbf{r})$ and $h(\mathbf{r})$ when each acoustic detector receives PA signals within a narrow cone. As shown in (12), $h(\mathbf{r})$ approaches infinity on the sphere whose center is the origin and whose radius is $ct_{max} - r_d$, and equals zero at other places. Based on the characteristics of the delta function and the origin-symmetric shape of $h(\mathbf{r})$, it is easy

Fig. 1. Detection geometry and PA signal integration.

to derive that $A(\mathbf{r}) * h(\mathbf{r})$ at position $\mathbf{r}$ equals to the integration of $A(\mathbf{r})$ over a sphere whose center is $\mathbf{r}$ and radius is $ct_{max} - r_d$, as shown in Fig. 1.

In short, $C(\mathbf{r})$ and $A(\mathbf{r}) * h(\mathbf{r})$ correspond to integrations on two spherical surfaces that do not perfectly overlap and are thereby only approximately equal. This misalignment is the physical origin of the error in the DR algorithm. It is also worth mentioning that these two spheres are tangential on the acoustic axis of each acoustic detector in the direction of $-\mathbf{r}$ (or $\mathbf{r}$). If the tissue volume is relatively small, the mismatch between these two spheres within the tissue will also be small, and so will be the error of this DR algorithm. This explanation is consistent with the conclusion of the previous mathematical derivation.

While the integration spherical surface of $C(\mathbf{r})$ has a radius of curvature dependent on variable $\mathbf{r}$, the integration spherical surface of $A(\mathbf{r}) * h(\mathbf{r})$ has a constant radius of curvature once t_{max} is set. We can exactly match the approximate spherical surface with the original spherical surface at one position. If the tissue volume is centered within the detection surface, it is reasonable to set the matching position at the origin by choosing $ct_{max} = 2r_d$.

One can further approximate the integration spherical shells to planes orthogonal to the acoustic axis [22], which is tantamount to a zero-order Taylor expansion of the cosine function of the acoustic detection angle. Although such an approximation reduces the spherical Radon transform to the planar counterpart, errors in the reconstructed images can be severe unless the tissue volume is extremely small.

3.3. Discrete Implementation

Here, we describe how to implement the DR algorithm in the most common 2-D applications, where PA signals are detected along a circle. The transducer used here should receive signals from the focal plane and reject out-of-plane signals because the acoustic detection is cylindrically focused. In this case, the convolution in (10) will approximately hold true in the 2-D case ($\mathbf{r}$ is reduced to a 2-D position vector).

During detection, the generated acoustic signal $p(\mathbf{r}_d, t)$, in which $\mathbf{r}_d$ is reduced to follow a circle, is sampled in both the space and time domains. Thus, the detected $p(\mathbf{r}_d, t)$ can be represented by an

$N_a \times N_t$ matrix, where N_a is the number of detection angles, and N_t is the number of sampled time points at each detection angle. Also, $S(\mathbf{r}_d, t)$ is represented by an $N_a \times N_t$ matrix.

Suppose we want to reconstruct an image with the resolution of $N \times N$ (stored as an $A(\mathbf{r})$ matrix), which represents a spatial size of $a \times a$ (located at the center of the detection circle). $h(\mathbf{r})$ can be represented by a matrix corresponding to the spatial size of $2r_d \times 2r_d$ (here, $ct_{max} = 2r_d$). Since the $A(\mathbf{r})$ matrix and $h(\mathbf{r})$ matrix will be convolved, each of their elements should represent the same discrete space interval. Therefore, $h(\mathbf{r})$ should be constructed as a $(N \cdot 2r_d/a) \times (N \cdot 2r_d/a)$ matrix, and $C(\mathbf{r})$, which is the convolution of $A(\mathbf{r})$ and $h(\mathbf{r})$, should be constructed as a $[N \cdot (2r_d/a + 1) - 1] \times [N \cdot (2r_d/a + 1) - 1]$ matrix. While calculating an element in the $C(\mathbf{r})$ matrix, the spatial coordinate of this element is transformed to the corresponding coordinate in the $S(\mathbf{r}_d, t)$ matrix, and then, the value of the nearest $S(\mathbf{r}_d, t)$ element is chosen (bilinear interpolation can be used for better accuracy at the cost of computation time). After all the elements of the $C(\mathbf{r})$ matrix are calculated, the $A(\mathbf{r})$ matrix, namely, the to-be-reconstructed image, can be obtained by using deconvolution.

The main steps in the DR algorithm are constructing $C(\mathbf{r})$ and deconvolution. To speed up the algorithm, $h(\mathbf{r})$ and the relationship between the variables of $C(\mathbf{r})$ and $S(\mathbf{r}_d, t)$ can be precalculated. The size of the $C(\mathbf{r})$ matrix is on the order of N^2; therefore, constructing $C(\mathbf{r})$ has a time complexity of $\Theta(N^2)$. The deconvolution step involves fast Fourier transformation (FFT), division in the frequency domain, and inverse FFT (IFFT). The time complexity of the division is $\Theta(N^2)$, and that of both FFT and IFFT is $\Theta(N^2 \log N)$. Thus, in total, the DR algorithm has a time complexity of $\Theta(N^2 \log N)$.

In comparison, back-projection algorithms and the delay-and-sum algorithm, i.e., two kinds of commonly used time-domain algorithms, add up all the N_a detected signals (with or without processing in the time domain) at each pixel of reconstructed image. Therefore, they have a time complexity of $\Theta(N_a N^2)$. Considering that N_a is normally of the same order as N for good image quality, the time complexity of these algorithms can be written as $\Theta(N^3)$. Therefore, the DR algorithm is much faster than back-projection algorithms and the delay-and-sum algorithm, especially when reconstructing high-resolution images. Moreover, as far as we know, the available frequency-domain algorithms for circular geometry either use a similar projection strategy [15] as these time-domain algorithms or calculate $\widetilde{A}(\omega)$ based on Bessel and Hankel functions [23]. They are even more time consuming and are, in fact, rarely used in practice.

4. Results and Discussion

The DR algorithm was applied to *in vivo* mouse brain imaging. The head of a mouse was depilated and then imaged with intact skull and skin. The experimental setup, as shown in Fig. 2, was similar to that of [17]. The Nd:YAG laser (LOTIS II LS-2137/2) generated pulses with a wavelength of 532 nm, a width of 16 ns, and a repetition rate of 10 Hz. PA signals were received by a 512-element circular transducer array whose diameter was 5 cm. The center frequency of the transducer was 5 MHz, and the bandwidth was greater than 80%. The signals were amplified, sampled at 40 MHz, and transferred to a computer for processing by the signal acquisition system.

The received PA signals (after deconvolving the transducer impulse response) are shown in Fig. 3(a). The two axes denote time and detection angle; the grayscale denotes normalized signal amplitude. The constructed space function $C(\mathbf{r})$ (also normalized) in the DR algorithm is shown in Fig. 3(b). Here, the parameter t_{max} is set to $2r_d/c$, and only the signals during 10–33 μs are used.

Fig. 4(a) and (b) show the images reconstructed by the exact back-projection algorithm [15] and the DR algorithm, respectively, when signals from all 512 detection angles are used. Then, we tested the robustness of these two algorithms by reducing the number of angles uniformly around the detection circle. Fig. 4(c) and (d) show the images reconstructed over 128 angles (selected every fourth one from the 512 angles). Fig. 4(e) and (f) show the images reconstructed over 64 angles. For comparison, we opened the skin of the mouse brain after PA imaging and took a photograph of the cerebral cortex [see Fig. 4(g)].

When reconstructed over 512 angles, the results of both algorithms are nearly identical and agree well with the photograph. The DR algorithm outperforms the back-projection algorithm when using
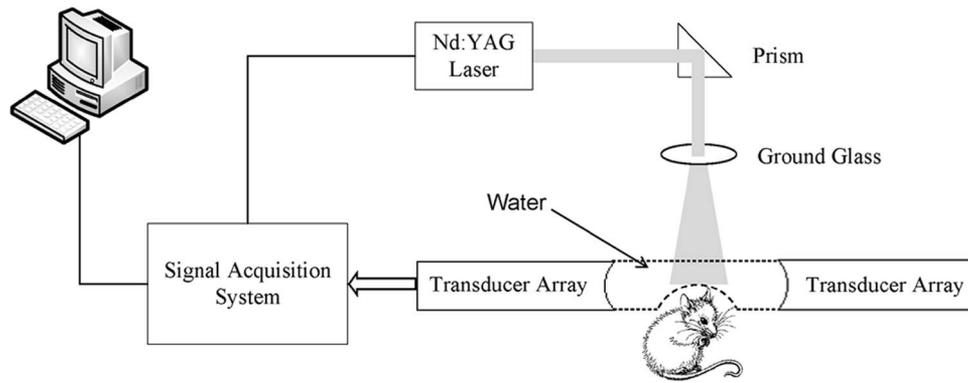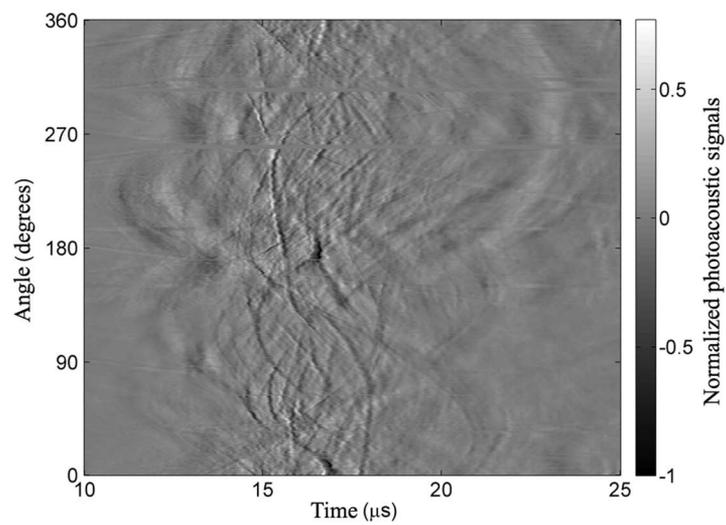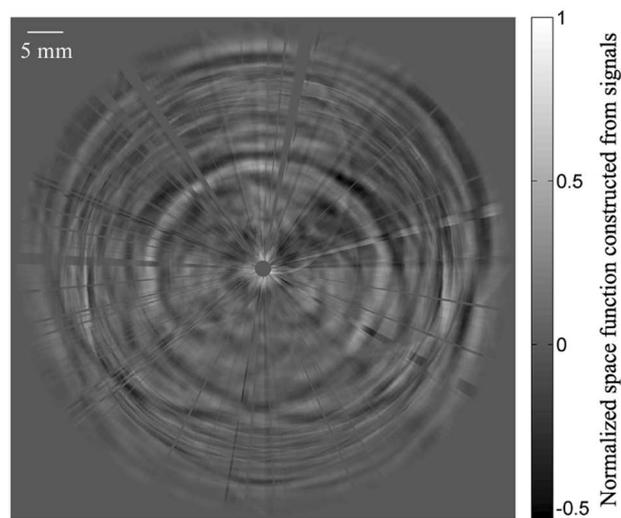
Fig. 2. Experimental setup.

Fig. 3. (a) Received PA signals and (b) constructed space function $C(\mathbf{r})$.
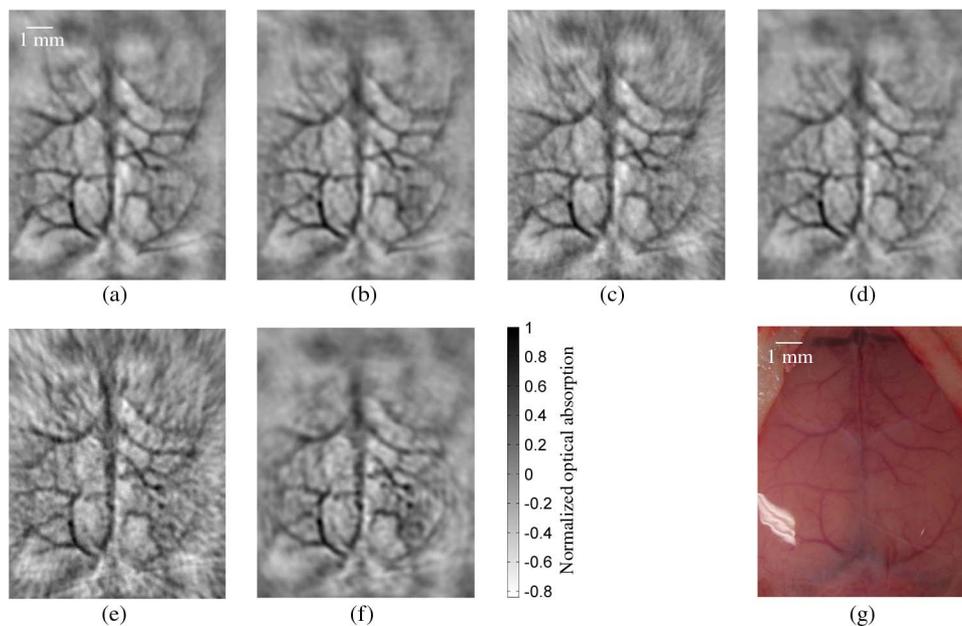
Fig. 4. *In vivo* and noninvasive reconstructed images using (a) back-projection over 512 angles, (b) deconvolution reconstruction over 512 angles, (c) back-projection over 128 angles, (d) deconvolution reconstruction over 128 angles, (e) back-projection over 64 angles, and (f) deconvolution reconstruction over 64 angles. (g) Photograph of the mouse cerebral cortex taken after imaging.

signals from fewer angles. It can be seen that the reconstructed image of the DR algorithm over 128 angles is as good as the image reconstructed over 512 angles, while the back-projection algorithm's result suffers from many vessel-like artifacts. When reconstructed over 64 angles, the image from the back-projection algorithm has very strong vessel-like artifacts that obscure real vessels. The image from the DR algorithm is blurred but generally better.

Here, we explain why the DR algorithm performs better. The exact back-projection algorithm uses an inverse formula, which ideally requires knowledge of the detected signals at every position of the detection circle; in practice, one can detect signals from only a limited number of angles. The back-projection algorithm does not project the undetected signals by assuming them to be zero. This assumption is in fact not true, and it introduces large errors if detection angles are sparse. In contrast, the DR algorithm is based on a valid forward model given by (10). The effectiveness of this forward model will not be affected by the number of detection angles. In fact, in $C(\mathbf{r})$ only the elements perfectly matching with the measurement points are exactly known. If the detection angles are too sparse, this model will be ill-conditioned and lead to unstable solutions, but it is a better starting point than an invalid inverse formula. Moreover, the DR algorithm's forward model is based on convolution, which can be directly and quickly solved using a deconvolution method without iterative calculations normally included in most forward-model-based methods. In our deconvolution, the unmeasured elements in $C(\mathbf{r})$ are estimated by the detected signals. The solution is not a least-squares one but is close.

The DR algorithm assumes, as mentioned above, that the object dimension is relatively small compared with the detection circle. In our experiment, the cross section of the mouse head is approximately elliptically shaped with a major axis of 2 cm, which is not much less than the detection diameter (5 cm). However, most vessels are within a 0.6×0.8 cm^2 region, roughly centered within the detection circle, and are clearly imaged. In practice, if an object is so large that the DR algorithm cannot reconstruct the full cross section clearly, we can limit the region of interest at the detection center for better image quality.

To compare the speeds of the back-projection and DR algorithms, we reconstructed images of a 2×2 cm^2 region (at the center of the transducer array) with different numbers of pixels. In practical
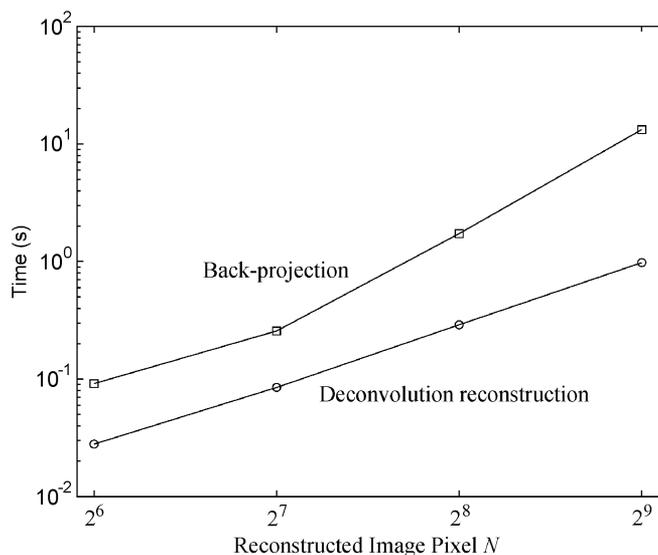
Fig. 5. Time costs of the back-projection algorithm and deconvolution reconstruction algorithm when reconstructing $N \times N$ images using signals from N detection angles.

applications, we reconstruct images with more pixels if we can achieve better spatial resolution; otherwise, adding pixels is meaningless because the added pixels contain little new spatial information. Moreover, more detection angles are normally required for better spatial resolution. Therefore, in order to investigate the calculation efficiencies of these two algorithms with different requirements of spatial resolution, the number of detection angles and the pixel resolution of reconstructed images in our calculation were varied simultaneously. In other words, we used signals from N detection angles to reconstruct an $N \times N$ image and recorded the time cost of each algorithm (Intel Core2 Duo CPU@3.00GHz, Matlab R2009a), where N was chosen to vary from 64, 128, 256, to 512. The results are shown in Fig. 5.

It can be seen that the time cost of the DR algorithm is much smaller than that of the back-projection algorithm. For each algorithm, the trend of increased time cost with N is consistent with the time complexity analysis in Section 3.3. When $N = 512$, the DR algorithm is about ten times faster than the back-projection algorithm. It can be predicted that the speed advantage of the DR algorithm is greater when $N > 512$. Moreover, according to these data, real-time imaging is possible only if $N \leq 256$ (in our system) if the DR algorithm is used. Since the DR algorithm presents stronger robustness for sparse detection angles, it should be preferably considered for real-time PA imaging in circular geometry.

5. Conclusion

Based on previous simulations, this work supplements the DR algorithm theoretically and validates it experimentally. The DR algorithm uses a convolution-based forward model, which is more effective than the inverse formula for sparse detection angles. Moreover, this model can be quickly solved by using a deconvolution-based method. Experimental results show that the DR algorithm provides image quality that is nearly identical to that of exact back-projection algorithm when using signals detected from 512 angles. When using 128 and 64 angles, the DR algorithm provides better images without vessel-like artifacts. It is also shown that the DR algorithm runs faster, agreeing well with the time complexity analysis. When designing a real-time PAT system, the number of detection angles cannot be very large, and the image-reconstruction algorithm should be fast; therefore, the DR algorithm becomes a good choice. In addition, by utilizing the DR algorithm in PAT systems, we can use fewer measurements for given image quality, thereby reducing experimental cost.

References

[1] L. V. Wang, "Multiscale photoacoustic microscopy and computed tomography," *Nat. Photon.*, vol. 3, no. 9, pp. 503–509, Sep. 2009.

[2] M. Xu and L. V. Wang, "Photoacoustic imaging in biomedicine," *Rev. Sci. Instrum.*, vol. 77, no. 4, pp. 41101–41122, Apr. 2006.

[3] A. G. Bell, "On the production of sound by light," *Amer. J. Sci.*, vol. 20, p. 305, 1880.

[4] J. J. Niederhauser, M. Jaeger, R. Lemor, P. Weber, and M. Frenz, "Combined ultrasound and optoacoustic system for real-time high-contrast vascular imaging *in vivo*," *IEEE Trans. Med. Imag.*, vol. 24, no. 4, pp. 436–440, Apr. 2005.

[5] H. F. Zhang, K. Maslov, G. Stoica, and L. V. Wang, "Functional photoacoustic microscopy for high-resolution and noninvasive *in vivo* imaging," *Nat. Biotechnol.*, vol. 24, no. 7, pp. 848–851, Jul. 2006.

[6] X. Wang, Y. Pang, G. Ku, X. Xie, G. Stoica, and L. V. Wang, "Noninvasive laser-induced photoacoustic tomography for structural and functional *in vivo* imaging of the brain," *Nat. Biotechnol.*, vol. 21, no. 7, pp. 803–806, Jul. 2003.

[7] C. Li and L. V. Wang, "Photoacoustic tomography of the mouse cerebral cortex with a high-numerical-aperture-based virtual point detector," *J. Biomed. Opt.*, vol. 14, no. 2, pp. 024 047, Apr. 2009.

[8] S. Hu, K. Maslov, V. Tsytsarev, and L. V. Wang, "Functional transcranial brain imaging by optical-resolution photoacoustic microscopy," *J. Biomed. Opt.*, vol. 14, no. 4, p. 040 503, Aug. 2009.

[9] L. V. Wang, X. M. Zhao, H. T. Sun, and G. Ku, "Microwave-induced acoustic imaging of biological tissues," *Rev. Sci. Instrum.*, vol. 70, no. 9, pp. 3744–3748, Sep. 1999.

[10] R. A. Kruger, K. D. Miller, H. E. Reynolds, W. L. Kiser, D. R. Reinecke, and G. A. Kruger, "Breast cancer in vivo: Contrast enhancement with thermoacoustic CT at 434 MHz—Feasibility study," *Radio.*, vol. 216, no. 1, pp. 279–283, Jul. 2000.

[11] M. Pramanik, G. Ku, C. H. Li, and L. V. Wang, "Design and evaluation of a novel breast cancer detection system combining both thermoacoustic (TA) and photoacoustic (PA) tomography," *Med. Phys.*, vol. 35, no. 6, pp. 2218–2223, Jun. 2008.

[12] R. G. M. Kolkman, P. J. Brands, W. Steenbergen, and T. G. van Leeuwen, "Real-time *in vivo* photoacoustic and ultrasound imaging," *J. Biomed. Opt.*, vol. 13, no. 5, p. 050510, Oct. 2008.

[13] Y. Xu, D. Feng, and L. V. Wang, "Exact frequency-domain reconstruction for thermoacoustic tomography—I: Planar geometry," *IEEE Trans. Med. Imag.*, vol. 21, no. 7, pp. 823–828, Jul. 2002.

[14] K. P. Kostli and P. C. Beard, "Two-dimensional photoacoustic imaging by use of Fourier-transform image reconstruction and a detector with an anisotropic response," *Appl. Opt.*, vol. 42, no. 10, pp. 1899–1908, Apr. 2003.

[15] M. Xu and L. V. Wang, "Universal back-projection algorithm for photoacoustic computed tomography," *Phys. Rev. E, Stat. Phys. Plasmas Fluids Relat. Interdiscip. Top.*, vol. 71, no. 1, p. 016706, Jan. 2005.

[16] C. G. A. Hoelen and F. F. M. Mul, "Image reconstruction for photoacoustic scanning of tissue structures," *Appl. Opt.*, vol. 39, no. 31, pp. 5872–5883, Nov. 2000.

[17] J. Gamelin, A. Maurudis, A. Aguirre, F. Huang, P. Guo, L. V. Wang, and Q. Zhu, "A real-time photoacoustic tomography system for small animals," *Opt. Express*, vol. 17, no. 13, pp. 10 489–10 498, Jun. 2009.

[18] J. Provost and F. Lesage, "The application of compressed sensing for photo-acoustic tomography," *IEEE Trans. Med. Imag.*, vol. 28, no. 4, pp. 585–594, Apr. 2009.

[19] C. Zhang and Y. Wang, "Deconvolution reconstruction of full-view and limited-view photoacoustic tomography: A simulation study," *J. Opt. Soc. Amer. A, Opt. Image Sci.*, vol. 25, no. 10, pp. 2436–2443, Oct. 2008.

[20] L. V. Wang and H.-I. Wu, *Biomedical Optics: Principles and Imaging.* Hoboken, NJ: Wiley, 2007.

[21] S. M. Riad, "The deconvolution problem: An overview," *Proc. IEEE*, vol. 74, no. 1, pp. 82–85, Jan. 1986.

[22] R. A. Kruger, P. Liu, Y. Fang, and C. R. Appledorn, "Photoacoustic ultrasound (PAUS)—Reconstruction tomography," *Med. Phys.*, vol. 22, no. 10, pp. 1605–1609, Oct. 1995.

[23] Y. Xu, M. Xu, and L. V. Wang, "Exact frequency-domain reconstruction for thermoacoustic tomography—II: Cylindrical geometry," *IEEE Trans. Med. Imag.*, vol. 21, no. 7, pp. 829–833, Jul. 2002.